



Supersonic cold spraying of titania nanoparticles on reduced graphene oxide for lithium ion battery anodes



Edmund Samuel^{a,1}, Jong-Gun Lee^{a,1}, Bhavana Joshi^a, Tae-Gun Kim^a, Min-woo Kim^a, Il Won Seong^b, Woo Young Yoon^{b,**}, Sam S. Yoon^{a,*}

^a School of Mechanical Engineering, Korea University, Seoul 136-713, Republic of Korea

^b Department of Materials Science & Engineering, Korea University, Seoul 02841, Republic of Korea

ARTICLE INFO

Article history:

Received 28 March 2017

Received in revised form

18 April 2017

Accepted 27 April 2017

Available online 28 April 2017

Keywords:

Supersonic spray coating

Titania

Reduced graphene oxide

Lithium ion battery

Anode

ABSTRACT

Titania (TiO₂) nanoparticles were uniformly distributed on and are well attached to reduced graphene oxide (rGO) by supersonic cold spraying. The process facilitated rapid production of lithium ion battery (LIB) anodes. Integration of TiO₂ with rGO not only enhanced the conductivity of the anode, but also prevented agglomeration of the titania nanoparticles, which facilitated uniform distribution of the nanoparticles and thus consistently reduced the electron diffusion length. Integration of rGO with TiO₂ widened the characteristic voltage range of the resulting rGO-TiO₂ composite (0.01–3 V) relative to that of pure TiO₂, which enhanced the capacity during the lithiation process. Therefore, the LIB cell exhibited superior performance with long cycle durations even under high current rate. The optimal weight ratio of rGO to TiO₂ was found to be 1:1, which produced a retention capacity of 203 mA h g⁻¹ at $N = 300$ cycle under a current rate of $1\text{ C} = 336\text{ mA g}^{-1}$. Rapid production of rGO/TiO₂ nanocomposites via supersonic cold spraying may facilitate commercialization of high-quality LIB cells.

© 2017 Published by Elsevier B.V.

1. Introduction

TiO₂ has been extensively studied for various applications, e.g., as high- k material [1] in integrated chips, solar cells [2], and gas sensors [3]. The rutile and anatase phases of TiO₂ show immense potential as anode materials for lithium ion batteries (LIBs) [4] and large-scale energy storage [5]. TiO₂ has also been used as a LIB electrode material because of its stable operation during lithiation and de-lithiation [6] and its good reversible capacity [7]. The volume change of TiO₂ during lithiation and de-lithiation is relatively small (<4%), which prevents the pulverization effect [5]. Consequently, TiO₂ provides excellent stability when used in LIB cells [8]. Thus, TiO₂ provides cycle longevity or retention capacity [9] and overall stable LIB cell operation.

To achieve stable Li-ion storage capability and safe LIB operation, the key factors to be considered are formation of the stable solid electrolyte interface (SEI) layer [10], volume change [11], and

the lithium insertion-extraction voltage [12]. The SEI is a passivation or impurity layer formed via decomposition of the electrolyte on anodes [12]. The SEI layer is immediately formed by the electrochemical reduction reaction during the very first cycle of the lithiation and delithiation processes. This SEI layer has relatively high electrical resistance however, the Li ions can pass through it during the insertion-extraction processes [10]. The formation of SEI layer consumes a significant amount of Li ions, which lowers the initial discharge voltage of the cycle. Because of random insertion of Li ions into the SEI layer, the layer grows in a random fashion and has a highly inhomogeneous composition. This inhomogeneous SEI layer traps Li ions and forms impurities such as LiF, LiOH, and other inorganic species [13]. Moreover, the anode material undergoes expansion and contraction processes, during which the electrode surface cracks; multiple SEI layers are formed over these cracks [13]. The adverse effects of SEI formation become more pronounced when the characteristic voltage of the anode material is low. For example, high capacity materials such as silicon, tin, and graphite have a relatively low characteristic voltage in the range of 0–0.5 V (versus Li/Li⁺) [14]. Furthermore, these high power materials also suffer from significant volume change during the lithiation/delithiation process.

As an alternative to the aforementioned materials, TiO₂ is

* Corresponding author.

** Corresponding author.

E-mail addresses: wyyoon@korea.ac.kr (W.Y. Yoon), skyyoon@korea.ac.kr (S.S. Yoon).

¹ These authors have contributed equally.

functional within a relatively high characteristic voltage range (above 1 V vs. Li⁺/Li) [15], which minimizes electrolyte decomposition and thus improves the safety of batteries and their suitability for hybrid electric vehicles (HEVs) [12,15]. This high characteristic voltage of TiO₂ is useful for minimizing the thickness of the SEI layer [16]. The TiO₂ is not only stable in the presence of electrolytes [9], but also retains a fairly large theoretical specific capacity (as high as 336 mA h g⁻¹) [12]. In addition, TiO₂ is nontoxic and its abundance in nature makes it commercially viable [17].

Various approaches have been developed for utilizing TiO₂ as an anode material for LIBs [14]. It is known that inclusion of rGO in TiO₂ improves the Li⁺ ion diffusion capacity [18] as well as the electronic conductivity of rGO-TiO₂ composites [18,19]. Hierarchical mesoporous composites of rutile TiO₂/C nanospheres were fabricated by Wang et al. [20], where the current rate of these materials was low (85 mA g⁻¹) and the first specific capacity was only 318 mA h g⁻¹. Cai et al. [21] fabricated hierarchically structured porous anatase TiO₂ and reported a specific capacity of 187 mA h g⁻¹ under a current rate of 170 mA g⁻¹. Kurc et al. [22] fabricated TiO₂/graphene oxide films and reported a specific capacity of 247 mA h g⁻¹ under a very low current rate of 5 mA g⁻¹.

None of the aforementioned studies utilized severe current rate [20]. In addition, the characteristic voltage of the composites was in the limited range of 1–3 V; thus, the cells employing these composites might still under-perform. Lastly, agglomeration of the TiO₂ nanoparticles during the lithiation/delithiation process reduces the number of electroactive sites, thereby preventing the realization of high LIB performance [23].

In view of these challenges, we tactically considered the incorporation of rGO into TiO₂ to accomplish Li-ion insertion even at a low characteristic voltage level, starting from 0.01 V, to enhance the lithiation and delithiation processes. Furthermore, we used supersonic cold spraying to uniformly distribute the TiO₂ nanoparticles on the rGO sheets at the instant of impact of these materials on a copper foil substrate. This supersonic impact also facilitates superior adhesion, which increases the interfacial electrochemical activity between the TiO₂ nanoparticles and rGO sheets. This type of strong material cohesion is expected to yield high storage capability at high current rate. Moreover, this supersonic spray coating approach facilitates the rapid production of large-scale LIB cells [24].

2. Experimental

2.1. rGO/TiO₂ composite

All the reagents, such as TiO₂ (Degussa P25, Germany), polyacrylonitrile (PAN, *M_w* = 150 kDa, Sigma-Aldrich), *N,N*-dimethylformamide (DMF, 99.8%, Sigma-Aldrich) and rGO (N002-PDR, Angstrom Materials) were used as received without further purification. The rGO/TiO₂ precursor solution was prepared by mixing respective concentrations of rGO and TiO₂ inside 40 ml of DMF. The PAN/DMF solution was prepared by dissolving PAN (8 wt%) with 10 ml of DMF. Then, 0.3 ml of the PAN/DMF solution was mixed with 40 ml of the rGO/TiO₂ precursor. The TiO₂ content was kept at 0.25 g for all precursor solutions, except for Case 4, which contained

Table 1
rGO/TiO₂ weight ratio.

Case No.	rGO/TiO ₂ (g)
1	0.00/0.25
2	0.15/0.25
3	0.25/0.25
4	0.25/0.00

100% rGO. The concentration variation is summarized in Table 1. The sonicated rGO/TiO₂ solution was then supplied to the supersonic stream of the spraying system. Fig. 1 shows a schematic of the supersonic spraying system comprising the air tank, in-line heater, supersonic nozzle, *x*-*z* stage, atomizer, and syringe pump. The details of the supersonic spraying system can be found in a previous report [24]. The precursor was supplied at a flow rate of 1.5 ml min⁻¹. The upstream chamber pressure and temperature of the supersonic stream were *P*₀ = 4 bar and *T*₀ = 250 °C, respectively for all cases. The nozzle-to-substrate distance was 7 cm, and all samples were prepared with a nozzle sweep number of *N* = 10. The prepared samples were annealed at 700 °C for 2 h in furnace under an argon environment.

2.2. Electrochemical tests

The annealed films were punched into a circular disc of 14 mm in diameter to be used as a working electrode while lithium metal was used as a counter electrode in an half cell. The mass of the active material (rGO/TiO₂) was fixed at 1.1 mg for all cases. The electrochemical tests were performed using CR-2032 type coin cells, which were assembled in a dry room using 1 M LiPF₆ in ethylene-carbonate (EC), dimethylcarbonate (DMC), and ethylmethyl carbonate (EMC) (1:1:1 by volume) (PuriEL, Soulbrain, Seongnam, South Korea) as the electrolyte and microporous polymer as the separator (Celgard 2400; Celgard, Chungbuk, South Korea). The assembled cells underwent the 24 h aging process to reach an equilibrium condition between the electrode and electrolyte. Then galvanostatic discharge/charge curves were measured using a WBCS3000 battery cycler system (WonATech, Seoul, South Korea). The voltage window used for the rate performance study was 0.01–3.0 V; the current rate was varied and the current was constant for long cycle duration. The specific capacity was calculated based on the total mass of the active materials, which are TiO₂, rGO/TiO₂, rGO for Case 1, 2 and 3, and 4, respectively. The prepared rGO/TiO₂ electrode shows immense potential as an anode material for lithium ion batteries.

3. Results and discussion

3.1. Material properties

A confocal Raman spectrometer (Jasco, NRS-3100) was used to analyze the rGO and TiO₂ content in the cold sprayed films. Fig. 2 presents a comparison of the Raman spectra of pure TiO₂ (Case

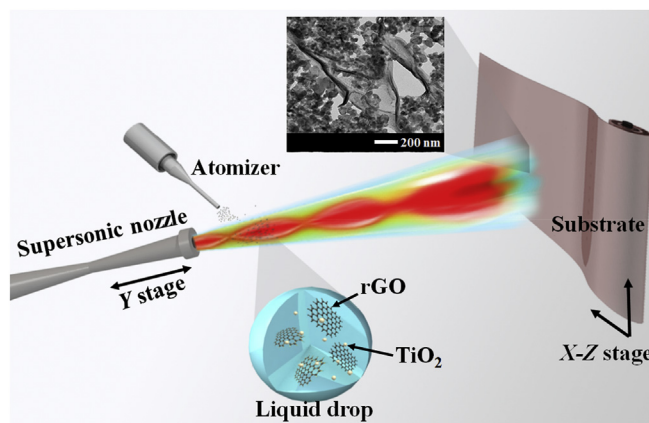


Fig. 1. Schematic representation of preparation of anode for lithium ion battery using cold-spray technique.

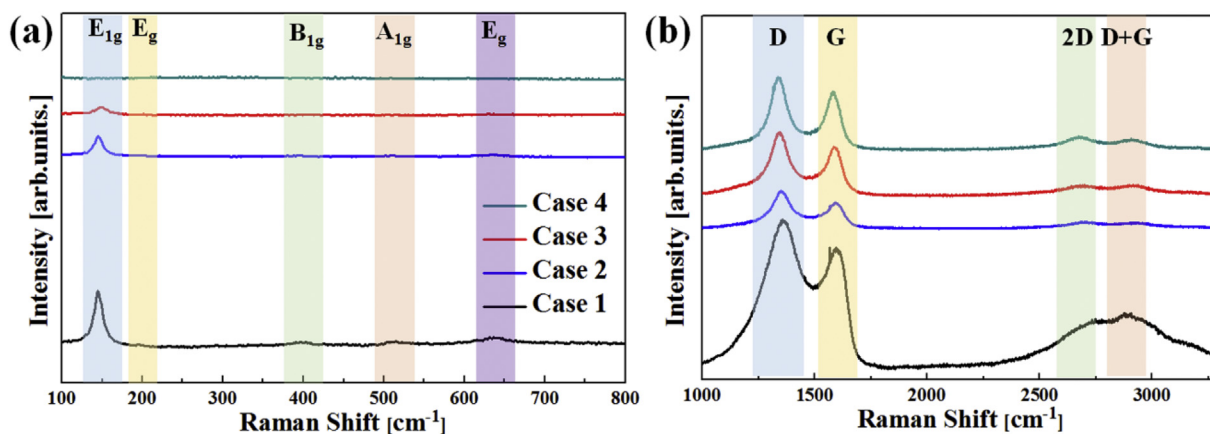


Fig. 2. Raman spectra of pure TiO₂ (Case 1), rGO-TiO₂ (Cases 2 and 3), and pure rGO (Case 4).

1), rGO-TiO₂ (Cases 2 and 3), and pure rGO (Case 4). The characteristic peaks of TiO₂ corresponding to the E_g(1), B_{1g}(1), A_{1g} + B_{1g}(1), and E_g(2) modes were clearly observed in Fig. 2a at 145, 198, 395, 513, and 633 cm⁻¹ respectively, which confirms the presence of the anatase phase in the samples. The addition of rGO shifted the E_g vibrational peak of TiO₂ from 145 cm⁻¹ to 150 cm⁻¹ (for Case 3). This blue shift is due to strong interaction of rGO and TiO₂ [25]. The presence of defects in the rGO-TiO₂ samples was confirmed by analysis of the D and G band, as shown in Fig. 2b. Disorder in the sp²-bonds of the carbon atoms was evident from the peak at 1335 cm⁻¹, corresponding to the D band. The peak at 1581 cm⁻¹ corresponds to the G band, assigned to the sp²-hybridized carbons. The changes in the D and G band peak positions and the I_D/I_G ratio are presented in Table 2. The D and G peaks observed in the case of pure TiO₂ are due to carbonization of PAN, indicating the presence of a relatively larger number of defects.

The X-ray diffraction (XRD, SmartLab, Rigaku) patterns of pure TiO₂ and the other cases are shown in Fig. 3. The diffraction patterns collected at room temperature by step scanning (0.01°) in the range of 20° < 2θ < 60° exhibit sharp peaks, indicating the good crystallinity of the samples. The diffraction peaks at 25.3°, 38.4°, 48°, 53.8, and 55.2° respectively correspond to the (101), (112), (200), (105), and (211) planes, confirming the presence of the anatase phase (JCPDS card no. 21-1272). The peaks at 27.41°, 36.01°, and 44° correspond to the (110), (101), and (210) planes, respectively, also confirming the presence of the rutile phase (JCPDS card no. 21-1276). The relative weight percentages of the anatase and rutile phases estimated from the intensity of the peaks at 25.06° (anatase) and 27.14° (rutile) were 81.6% and 18.4%, respectively [26]. The diffraction peak for graphene should be present at 25.71°, but is in general difficult to identify. However, the presence of graphene was previously confirmed by the Raman peaks in Fig. 2. The peaks assigned to Cu in Fig. 3 are due to the presence of the copper substrate.

X-ray photoelectron spectra (Theta Probe Base System, Thermo Fisher Scientific Co.) were acquired to confirm the presence of elements and their chemical states. The survey spectrum (Fig. 4a)

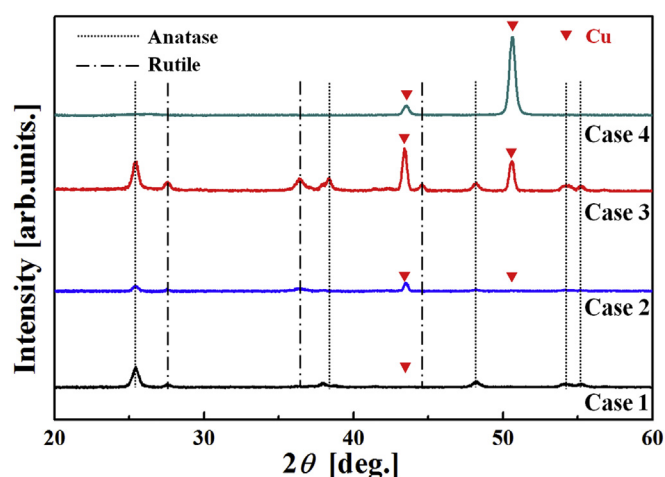


Fig. 3. XRD patterns for pure TiO₂ (Case 1), rGO-TiO₂ (Cases 2 and 3), and pure rGO (Case 4).

shows peaks that confirm the presence of Ti, O, and C in the films. The peaks of Ti 2p_{1/2} and Ti 2p_{3/2} at 464.8 and 459.1 eV in Fig. 4b confirm the anatase phase of TiO₂ and the energy difference between the two peaks is 5.7 eV, which implies the presence of the Ti⁴⁺ state. No other peaks in conjunction with the oxidation state of Ti were observed in the deconvoluted spectrum, which confirms the presence of TiO₂ in the films. The deconvoluted O1s spectrum (Fig. 4c) shows two peaks centered at 530.2, 531.4 eV, and 532.5 eV, corresponding to the Ti–O–Ti, C–O and O–H groups, respectively. Fig. 4d shows the C1s characteristics; after deconvolution, three peaks appeared at 284.3, 285.9, and 289.2 eV, attributed to graphitic carbon (C=C), C–O, and C=O bonds, respectively [27]. The intensities of the other carbon atoms corresponding to C–O and C=O were significantly weaker than that corresponding to C=C, confirming the presence of rGO. The atomic weight percent of TiO₂ and rGO for Case 3 confirms that the weight percent was not changed even after the annealing process.

The morphology and particle size of the rGO-TiO₂ composites was tailored in the best possible way via supersonic spraying due to the high velocity impact of the particle on the substrate. Fig. 5 shows the surface morphology observed by field emission scanning electron microscopic (FE-SEM, S-5000, Hitachi, Ltd.) analysis of pure TiO₂ (Case 1), the rGO-TiO₂ composites (Case 2 and 3), and pure rGO (Case 4). Agglomerated TiO₂ nanoparticles were clearly observed in Case 1. Agglomeration hinders the lithiation process

Table 2
D and G band Peak positions and its intensity ratio.

Case	D peak position [cm ⁻¹]	G peak position [cm ⁻¹]	I _D /I _G
1	1356	1594	1.37
2	1345	1585	1.22
3	1337	1583	1.29
4	1335	1581	1.05

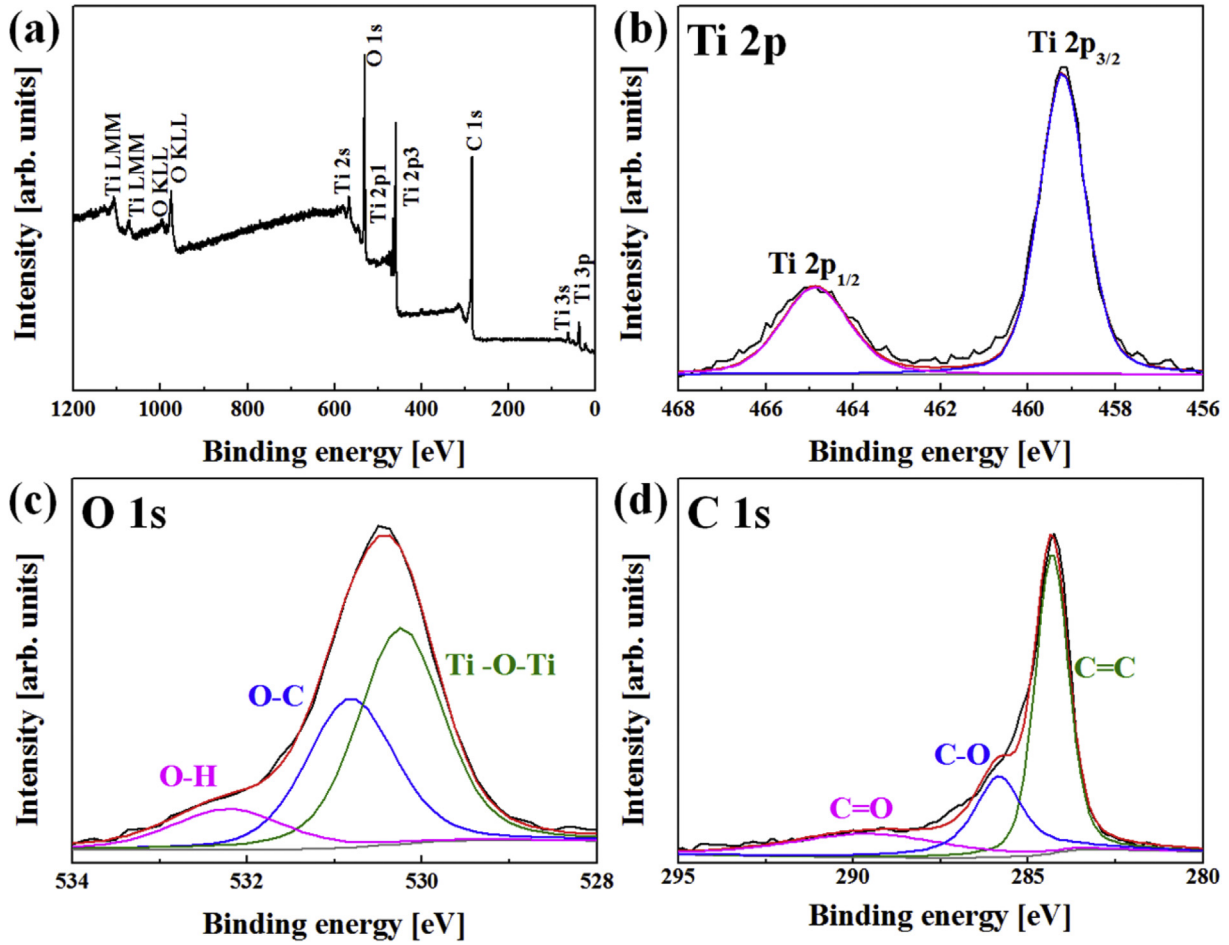


Fig. 4. XPS spectra of rGO-TiO₂ (Case 3): (a) survey spectrum; deconvoluted spectra of (b) Ti2p, (c) O1s, and (d) C1s.

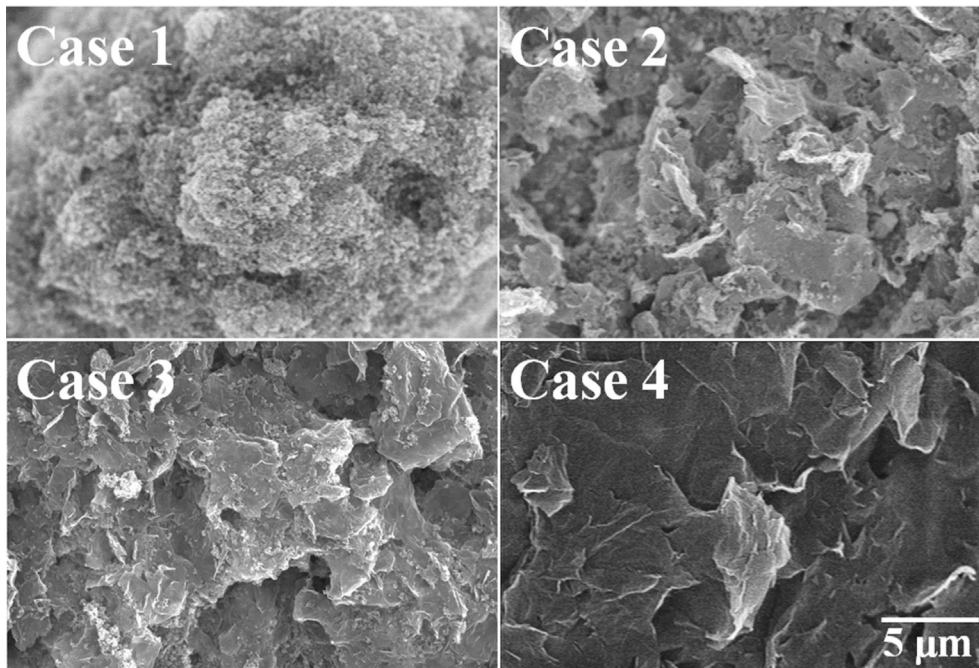


Fig. 5. Surface morphology for pure TiO₂ (Case 1), rGO-TiO₂ (Cases 2 and 3), and pure rGO (Case 4).

due to the reduced electroactive sites [23]. In Case 2, the TiO_2 nanoparticles were spread excessively over the rGO sheets, and also showed some degree of agglomeration. In Case 3, the TiO_2 nanoparticles were uniformly distributed over the rGO sheets; the rich network between rGO and TiO_2 provides a pathway for efficient movement of the Li^+ ions, which should enhance the retention capacity of the LIB cell. Pure rGO (Case 4) shows well-stretched graphene sheets distributed homogeneously over the substrate. However, in the absence of TiO_2 , rGO shows poor performance due to restacking [28].

The surface morphology, microstructure, and crystallinity of rGO- TiO_2 were investigated by transmission electron microscopy (TEM, JEM 2100F, JEOL Inc.). The high resolution TEM (HR-TEM) images in Fig. 6 confirm the morphological characteristics of the rGO- TiO_2 composites. The TiO_2 nanoparticles were well distributed over the rGO sheets; this uniform distribution was facilitated by supersonic impact at the substrate. Because agglomerated TiO_2 nanoparticles collided with the rGO sheet at a supersonic speed, the agglomerated TiO_2 nanoparticles fragmented into pieces and were uniformly redistributed over the rGO sheet, which is a desirable feature for LIB anodes. Fig. 6a confirms the uniform distribution of the TiO_2 particles on the rGO sheets. The SAED pattern (inset in Fig. 6a) shows several diffraction rings, among which the red circle (200 and 215) corresponds to rGO and the blue ring pattern of the (101) plane confirms the presence of the anatase phase. Further, elemental mapping of the rGO- TiO_2 composite confirms the presence of carbon, titanium, and oxygen.

3.2. Anode performance

Li^+ insertion and extraction in TiO_2 during the discharging/

charging process can be expressed by the reversible reaction mechanism as below: [14].



According to Eq. (1), the kinetics of Li^+ insertion and extraction can provide a maximum theoretical capacity for lithium storage of 336 mA h g^{-1} when 1 mol of Li^+ is inserted per TiO_2 molecule. However, the insertion coefficient is restricted to 0.5 for bulk anatase TiO_2 [29], thereby reducing the practical lithium storage capacity of TiO_2 (168 mA h g^{-1}) [21]. The capacity can be improved by utilizing TiO_2 nanoparticles.

Fig. 7a shows the rate capability of the fabricated anodes in the current rate range from 0.1 C to 2 C, where $1 \text{ C} = 336 \text{ mA g}^{-1}$. The first ($N = 1$) discharge capacities were 383, 434, 487, and 246 mA h g^{-1} for Cases 1, 2, 3, and 4, respectively. As illustrated earlier in Eq. (1), the use of nanoparticulate TiO_2 (Case 1) caused a slight increase in the theoretical capacity of TiO_2 as compared to the use of bulk TiO_2 . The presence of rGO in Case 2 improves the conduction pathways between TiO_2 and the current collector and causes efficient electron transport along with effective charge separation, resulting in improved capacity compared to Case 1 [30]. The integration of rGO with TiO_2 in Case 2 resulted in better capacity than Case 1. However, at higher current rate, Case 2 shows very small increment in capacity in comparison to Case 1. Case 3 provided better performance compared to the other cases due to efficient wrapping of TiO_2 with rGO, which reduces agglomeration of TiO_2 and restacking of graphene; rGO provides a synergetic effect and improving the capacity. The Case 3, could be withstood at higher current rate (2C) and there was better capacity retention after completing the entire $N = 60$ cycles. This capacity retention is

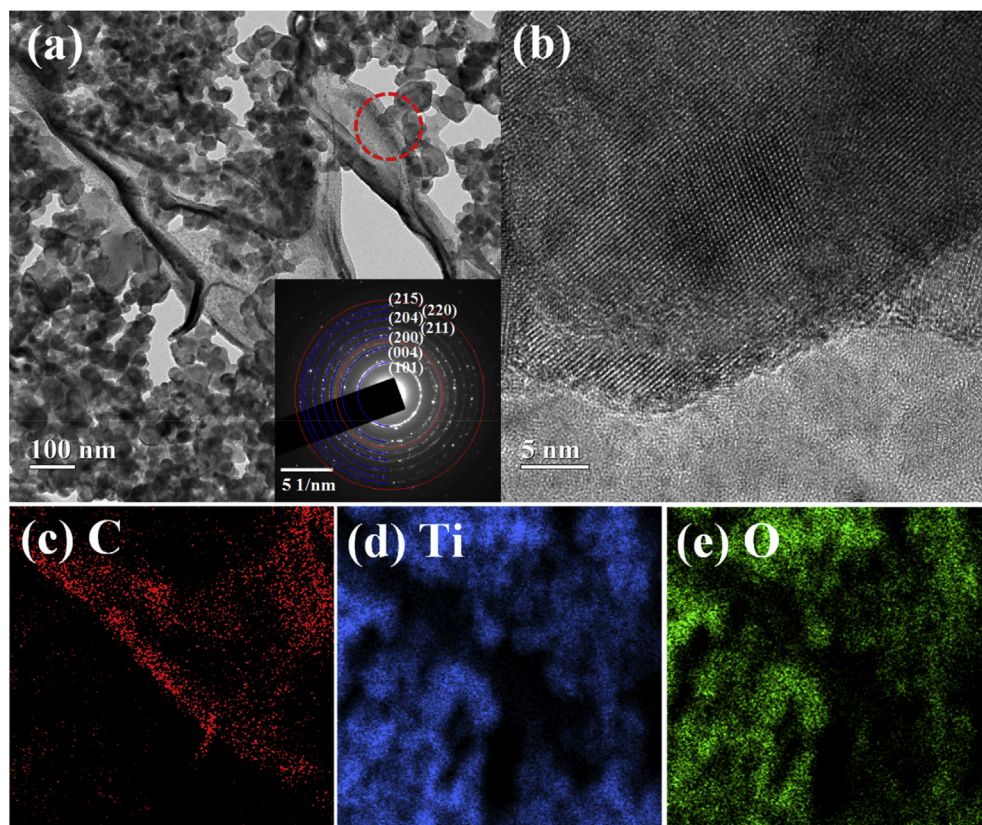


Fig. 6. TEM images of rGO- TiO_2 composite (Case 3): (a) Selected area electron diffraction (SAED) pattern (inset), (b) HR-TEM of the circled region in (a), and (c–e) Elemental mapping.

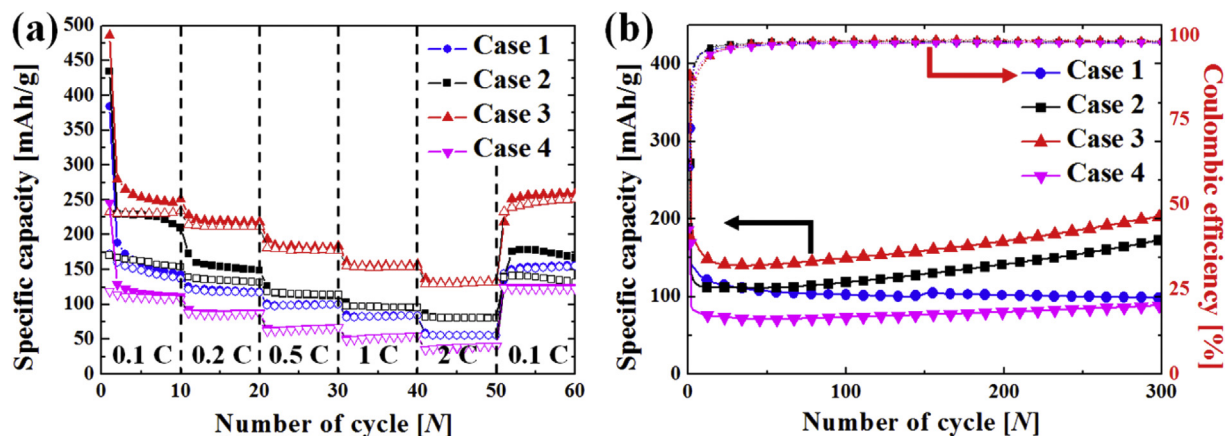


Fig. 7. (a) Rate capability over $N = 60$ cycles under various current rates. (b) Long term capability over $N = 300$ cycles under the current rate of 1 C.

higher (compared to the other cases) because of the optimal weight combination of rGO and TiO_2 . The capacity retention in Case 3, where rGO: TiO_2 is 1:1, was almost 95% ($N = 60$) relative to the first reversible capacity, which is better than the capacity retention of 80% ($N = 60$) for Case 1 (TiO_2) (Fig. 7). Case 4 (pristine rGO) shows lower battery capacity due to aggregation of the graphene sheets at higher current rate, which reduces the distance between sheets. Thus, Case 4 underperforms significantly as compared to the other cases. Consequently, the integration of TiO_2 with graphene reduces the restacking of graphene [31] and increases the lithium storage capacity. The sudden decrease in the capacity after $N = 1$ is attributed to SEI formation in all cases. Thus, SEI formation contributes in gaining the high capacity value initially [32], but reduces the initial Coulombic efficiency as shown in Fig. 7b. At a reduced current rate, a lower Coulombic efficiency was observed in Case 2 and 3 because of reduced activities of TiO_2 reaction and increased trapping of Li-ions [33].

Thus, it is inferred that nanosized TiO_2 particles are present in Case 3, which reduces the Li^+ diffusion distance and increases the surface/interfacial space for lithium storage. Furthermore, the contribution of the TiO_2 particles due to wrapping of reduced graphene oxide provides an improved and enhanced conductive network, facilitating better electrochemical processes for lower current rate as well as higher current rate.

In Table 3 for $N = 1$ at 0.1 C, the discharge capacity for Case 1 (pure TiO_2) is 384 mA h g^{-1} what that for Case 4 (pure rGO) is 246 mA h g^{-1} . In theory, if TiO_2 and rGO were mixed together by the same weight percent (Case 3), the theoretical capacity would be 630 mA h g^{-1} . In this scenario, the capacity contribution by TiO_2 would be about 61% ($384/630$) while that by rGO would be about 39% ($246/630$). We hypothesize that this contribution ratio retains in an actual case. For example, in Case 3, the actual discharge capacity is 487 mA h g^{-1} . Extrapolating the hypothesis, the TiO_2 contribution would be 61% of 487 mA h g^{-1} , which is 297 mA h g^{-1} .

Table 3
Discharge capacity contribution of rGO and TiO_2 at various cycles and current rates.

Case	Discharge capacity [$\text{mA} \cdot \text{h} \cdot \text{g}^{-1}$]								
	$N = 1$ at 0.1 C			$N = 31$ at 1 C			$N = 60$ at 0.1 C		
	Total	TiO_2	rGO	Total	TiO_2	rGO	Total	TiO_2	rGO
Case 1	384	384	0	85	85	0	157	157	0
Case 2	435	265	170	103	64	39	167	93	74
Case 3	487	297	190	162	101	61	260	145	115
Case 4	246	0	246	52	0	52	124	0	124

Likewise, the rGO contribution would be 190 mA h g^{-1} . This rough estimation has been assumed for all cases at all current densities in Table 3. As a result, the TiO_2 contribution is about in the range of 55–62% of the total capacity and thus the corresponding rGO contribution is 45–38%. Overall, the TiO_2 contribution is greater than the rGO contribution. At higher cycles, the TiO_2 contribution was slightly diminished probably because of the pulverization process of TiO_2 nanoparticles.

Hence, the long cycle performance achieved for all Cases at the high current rate of $1 \text{ C} = 336 \text{ mA g}^{-1}$ and the discharge capacity for $N = 1$ –300 are shown in Fig. 7b. The long term cycles clearly reveals the stability is highly improved by using rGO as it is observed in Fig. 7b Case 4 (pristine rGO case) shows almost linearity throughout the cycles. However, for Case 1 (pure TiO_2) the capacity decreases with increase in number of cycles. Furthermore, the rGO/ TiO_2 composite (Case 2 and 3) do not show fall in capacity during long-term cycle performance which may be attributed to the synergistic effect of rGO and TiO_2 . The first discharge capacity for Case 3 was 385 mA h g^{-1} and the first reversible capacity was 194 mA h g^{-1} . The capacity declined further up to $N = 30$ due to slower diffusion of the Li ions, which generates concentration polarization in the electrode at high current rate [34]. However, with further lithiation/delithiation, the capacity increased because of the increased TiO_2 reaction activities [27], providing a retention capacity of 204 mA h g^{-1} . The synergistic effect of the TiO_2 nanoparticles and rGO provides high electronic conductivity and high surface area [28,31], leading to superior electrochemical performance. Case 3 demonstrates excellent performance at high current and better stability during long-duration cycling with a high battery capacity for $N = 300$.

The discharge/charge cycles $N = 1$ and 2 at 34 mA g^{-1} and $N = 50$ at 672 mA g^{-1} are shown in Fig. 8 for all cases. Li^+ insertion in anatase TiO_2 can be divided into three different stages [35]. The first stage is characterized by a monotonous voltage drop from the open-circuit voltage to 1.79 and 1.78 V, respectively, for the first cycle for Cases 1 and 2 (Fig. 8a and b), indicating lithium insertion in the electrode. Fig. 8c–d, shows sharper voltage drops to 1.75 and 0.94 V for Cases 3 and 4, respectively. This indicates better electronic conductivity of the anode material due to the higher proportion of rGO in Case 3. However, for Cases 1–3, the second stage is marked by a horizontal plateau region corresponding to lithiation/delithiation. In this horizontal plateau region, Li^+ is inserted into the vacant octahedral sites of the TiO_2 lattice. The intercalation of Li ions into TiO_2 forms two phases; one is tetragonal $\text{Li}_{0.01}\text{TiO}_2$ (lithium poor) and the other is orthorhombic $\text{Li}_{0.6}\text{TiO}_2$ (lithium rich) [27]. The horizontal plateau is obtained when these two

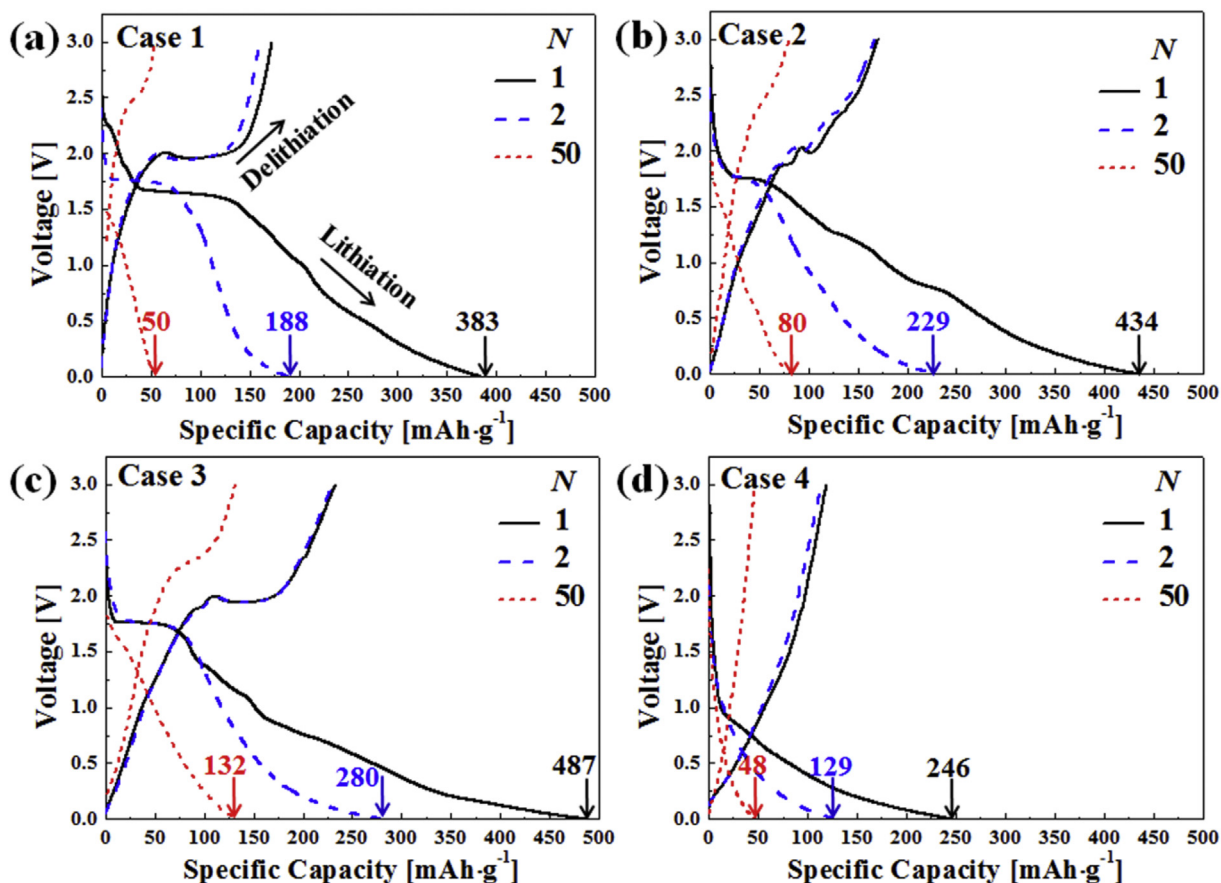


Fig. 8. Discharge/charge curves for (a) Case 1, (b) Case 2, (c) Case 3, and (d) Case 4. The current rate was 34 mA g^{-1} for $N = 1$ and 2. The current rate was 672 mA g^{-1} for $N = 50$.

phases are in equilibrium [36]. Thus, in the charge-discharge profile for Case 3, which shows a broader horizontal plateau, the two phases are not in equilibrium, and the dominance of the orthorhombic $\text{Li}_{0.6}\text{TiO}_2$ phase might account for the higher battery capacity [28]. The horizontal plateaus are not observed in Fig. 8d due to the absence of TiO_2 that shifts the voltage drop to 0.94 V suggesting activation polarization. The third stage is an elongated region, indicating increased Li insertion along with SEI layer formation due to the high surface area of rGO [28] and small crystallite size of TiO_2 [5].

For Case 4 (Fig. 8d), the shape of the discharge/charge curves matches that reported for graphene-based anodes [37]. The large irreversible capacity loss of 50% during the first cycle is attributed to the formation of a SEI layer on rGO, along with the reaction of the residual oxygen-containing functional groups on graphene with Li^+ ions. However, thereafter, the Coulombic efficiency increased to 94.7%, indicating good reversibility of the electrochemical reactions.

The differential capacity (dQ/dV) is used to observe the electrochemical changes occurring in the Li-ion battery. Most significantly, the phase-change of the transition metal oxides, observed through the electrochemical reactions emerging at different potentials and the variation in the peak positions, reveals detailed information regarding the electrode under study. The differential capacity was normalized relative to the initial capacitance, $Q_0 = 1000 \text{ mAh}$. Thus, the electrochemical reactions of the battery were studied by using the normalized differential capacitance ($(1/Q_0)dQ/dV$) from the discharge curves. Fig. 9 presents the dQ/dV data for $N = 1$ and 2 for Cases 1–4 at a constant current of 34 mA g^{-1} . The lithiation or discharge curve shows a peak at 1.73 V at $N = 1$ for Case

1, related to lithium ion insertion in TiO_2 [38]. However, for Case 4 (Fig. 9d), the peak at 0.58 V indicates the insertion of Li^+ as well as SEI formation.

The variation of the composite performance with the use of different TiO_2/rGO ratios (Case 2 and Case 3) was also analyzed. Fig. 9b and c shows the data for Case 2 and Case 3, respectively; the peaks at 0.77 and 0.72 V for $N = 1$ are attributed to SEI layer formation, while the peaks at 1.75 and 1.76 V indicate Li^+ insertion in TiO_2 . In both cases, two separate peaks were observed with respective potential differences of 0.98 and 1.04 V. The variation in SEI peak position in rGO based Cases 2–4 at 0.77, 0.72 and 0.58 V could be due to attached functional group to rGO and formation of partially irreversible SEI layer [11,39]. However, for Cases 2 and 3, the peaks around 0.77 and 0.72 V disappeared at $N = 2$. The disappearance of the peaks in the second cycle indicates that SEI formation was completed during the very first discharging/charging cycle. The dominant peaks in the voltage ranges of 0.77–1.75 V (Case 2) and 0.72–1.76 V (Case 3) correspond to the plateau region of the discharge/charge profiles shown in Fig. 8 for the respective cases. These plateaus demonstrate the multiphase nature of the intercalation/deintercalation process [40].

The kinetic process of the fabricated electrodes are studied through the electrochemical impedance spectroscopy (EIS). The Nyquist data were analyzed using the Randle's equivalent circuit model, as depicted in Fig. 10. In Table 4, the corresponding resistance values were computed, where R_s is the solution resistance and R_{ct} is charge transfer resistance. CPE is the constant phase element related to the electrode/electrolyte interface capacitance. W is the Warburg diffusion impedance associated with the kinetics of the Li-ions diffusion. The semicircle pattern of Z' vs. Z'' in shape

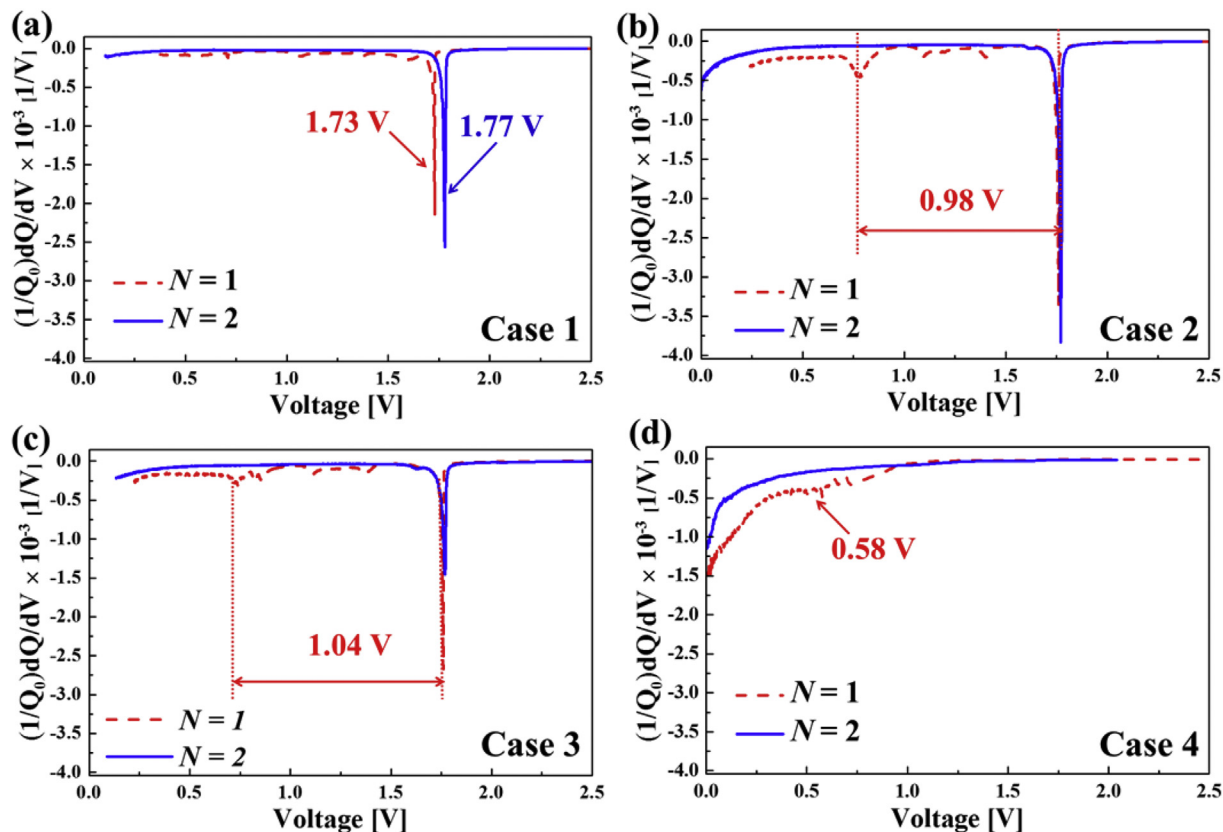


Fig. 9. Differential capacitance during discharge (lithiation) for (a) Case 1, (b) Case 2, (c) Case 3, and (d) Case 4 under the current rate of 34 mA g^{-1} .

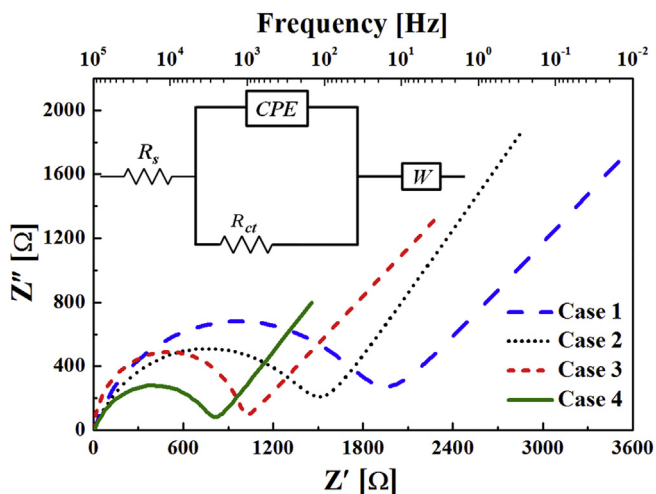


Fig. 10. Nyquist plots for electrochemical impedance spectroscopy for Cases 1–4.

Table 4
Solution impedance and charge transfer impedance for Cases 1–4.

Sample	Solution impedance, R_s , [Ω]	Charge transfer impedance, R_{ct} , [Ω]
Case 1	7.3	1556
Case 2	7.1	1147
Case 3	4.5	957
Case 4	11.9	674

implies the nature of the electrically conducting materials for all cases in Fig. 10. In Table 4, it is evident that the electrical

conductivity increases (or the resistance decreases) with increasing the rGO content. As nearing the lower frequency range, a linear behavior is observed between Z' vs. Z'' , which is described as the Warburg impedance. The linearity in the Warburg regime in the lower frequency range implies an excellent morphology of the samples, as in Fig. 6a. This linearity also implies that Li-ions are well diffusing across the electrolyte/electrode interface during the long-term cycle, as demonstrated in Fig. 7b.

Lithium ion transport has improved due to the electrical conductivity enhancement by rGO flakes. The Nyquist plot implies the reduction in Z' from Cases 1 to 3, which indicates the diffusion length has reduced and therefore the faster diffusion of Li-ions was promoted. However, for Case 4, even if having a lower impedance (Z'), the fabricated film lack the reaction sites due to the absence of TiO_2 nanoparticles. Therefore, Case 4 is not capable of storing a large amount of Li-ions and has the highest solution resistance value of 11.9Ω . A thin SEI layer was formed on rGO flakes in Case 4, which also traps Li-ions greatly, lowering the specific capacity. The features of the rGO/ TiO_2 composites prepared herein were compared under similar conditions, as presented in Table 5 [12,20–22,27]. The LIB storage capacity at high current rate and the capacity retention were very significant. Thus, the rGO/ TiO_2 composite electrodes fabricated by the fast, facile supersonic cold spray coating method are promising as LIB anodes.

4. Conclusions

The rGO/ TiO_2 hybrid films were fabricated using the cold spray technique. The composite electrode with a rGO/ TiO_2 ratio of 1:1 showed improved lithium storage capacity compared to that with pristine TiO_2 . The composite also showed superior capacity

Table 5Comparison of cold sprayed rGO/TiO₂ composite with the similar composite results in literature.

Composition	Electrode material preparation method	First Discharge capacity [mA.h.g ⁻¹]	First reversible capacity [mA.h.g ⁻¹]	Retention Capacity (Nth) [mA.h.g ⁻¹]	Current rate [mA.g ⁻¹]	Ref.
TiO ₂ spheres	Chemical (nanosphere)	187	186	178(100)	170	[21]
Carbon/rGO/TiO ₂	Solvothermal (nanosheet)	181	181	273 (500)	100	[27]
Carbon/TiO ₂	Electrochemical (nanoparticles)	211	197	171 (200)	84	[12]
Carbon/TiO ₂	Solution synthesis (nanospheres)	318	192	186 (50)	85	[20]
Graphene oxide/ TiO ₂	Hydrothermal (nanoparticle)	247	245	240 (10)	5	[22]
rGO/TiO₂	Supersonic Cold spray	385	193	203 (300)	336	Present

retention of 204 mA h g⁻¹ after 300 cycles at 1 C. The enhanced performance is due to the good coverage of the rGO sheets with TiO₂, which expedites electron transport and minimizes the agglomeration of TiO₂. Thus, cold-spray-coated rGO/TiO₂ is a promising anode material for LIBs.

Acknowledgement

This research was supported by the Technology Development Program to Solve Climate Changes of the National Research Foundation (NRF) funded by the Ministry of Science, ICT & Future Planning (2016M1A2A2936760) and NRF-2017R1A2B4005639. This work was supported by the Industrial Strategic Technology Development Program (10045221) funded by the Ministry of Knowledge Economy (MKE, Korea).

References

- [1] M.Z.R. Khan, D. Hasko, M. Saifullah, M. Welland, *J. Phys. Condens. Matter* 21 (2009) 215902.
- [2] J.T.-W. Wang, J.M. Ball, E.M. Barea, A. Abate, J.A. Alexander-Webber, J. Huang, M. Saliba, I.N. Mora-Sero, J. Bisquert, H.J. Snaith, *Nano Lett.* 14 (2013) 724–730.
- [3] H. Wang, L. Chen, J. Wang, Q. Sun, Y. Zhao, *Sensors* 14 (2014) 16423–16433.
- [4] X. Fu, L. Shi, C. Fan, S. Yu, G. Qian, Z. Wang, *Electrochim. Acta* 190 (2016) 25–32.
- [5] Z. Xiu, X. Hao, Y. Wu, Q. Lu, S. Liu, *J. Power Sources* 287 (2015) 334–340.
- [6] Y. Tang, L. Hong, Q. Wu, J. Li, G. Hou, H. Cao, L. Wu, G. Zheng, *Electrochim. Acta* 195 (2016) 27–33.
- [7] T. Zhou, Y. Zheng, H. Gao, S. Min, S. Li, H.K. Liu, Z. Guo, *Adv. Sci.* 2 (2015) 1500027.
- [8] L. Yang, X. Zhang, Y. Li, F. Hao, H. Chen, M. Yang, D. Fang, *Electrochim. Acta* 155 (2015) 272–278.
- [9] B. Wang, H. Xin, X. Li, J. Cheng, G. Yang, F. Nie, *Sci. Rep.* 4 (2014) 3729.
- [10] S.J. An, J. Li, C. Daniel, Mohanty D, Nagpure S, D.L. Wood III, *Carbon* 105 (2016) 52–76.
- [11] S.K. Park, H.-K. Kim, K.C. Roh, K.-B. Kim, H.S. Park, *CrystEngComm* 18 (2016) 6049–6054.
- [12] J. Chen, H. Hou, Y. Yang, W. Song, Y. Zhang, X. Yang, Q. Lan, X. Ji, *Electrochim. Acta* 164 (2015) 330–336.
- [13] L.H. Huang, Z.H. Min, Q.Y. Zhang, *Rev. Adv. Mater. Sci.* 36 (2014) 13–20.
- [14] X. Su, Q. Wu, X. Zhan, J. Wu, S. Wei, Z. Guo, *J. Mater. Sci.* 47 (2012) 2519–2534.
- [15] W.W. Terrence Xu, Mikhail L. Gordin, Donghai Wang, Daiwon Choi, *J. Miner. Met. Mater. Soc.* 62 (2010) 24–30.
- [16] G.C. Hui Wu, Jang Wook Choi, Ill Ryu, Yan Yao, Matthew T. McDowell, Seok Woo Lee, Ariel Jackson, Yuan Yang, Liangbing Hu, Yi Cui, *Nat. Nanotechnol.* 7 (2012) 310–315.
- [17] Y. Yeo, J.W. Jung, K. Park, I.D. Kim, *Sci. Rep.* 5 (2015) 13862.
- [18] K. Zhou, Y. Zhu, X. Yang, X. Jiang, C. Li, *New J. Chem.* 35 (2011) 353–359.
- [19] H. Fang, L. Zhao, W. Yue, Y. Wang, Y. Jiang, Y. Zhang, *Electrochim. Acta* 186 (2015) 397–403.
- [20] W.L. Wang, J.-Y. Park, V.H. Nguyen, E.M. Jin, H.-B. Gu, *Ceram. Int.* 42 (2016) 598–606.
- [21] Y. Cai, H.-E. Wang, J. Jin, S.-Z. Huang, Y. Yu, Y. Li, S.-P. Feng, B.-L. Su, *Chem. Eng. J.* 281 (2015) 844–851.
- [22] B. Kurc, K. Siwińska-Stefańska, P. Jakóbczyk, T. Jesionowski, *J. Solid State Electrochem.* 20 (2016) 1971–1981.
- [23] H. Cao, B. Li, J. Zhang, F. Lian, X. Kong, M. Qu, *J. Mater. Chem.* 22 (2012) 9759.
- [24] D.-Y. Kim, S. Sinha-Ray, J.-J. Park, J.-G. Lee, Y.-H. Cha, S.-H. Bae, J.-H. Ahn, Y.C. Jung, S.M. Kim, A.L. Yarin, S.S. Yoon, *Adv. Funct. Mater.* 24 (2014) 4986–4995.
- [25] H. Liu, K. Cao, X. Xu, L. Jiao, Y. Wang, H. Yuan, *ACS Appl. Mater. Interfaces* 7 (2015) 11239–11245.
- [26] H. Yoon, B. Joshi, S.H. Na, S.S. Yoon, *J. Electrochem. Soc.* 159 (2012) H823–H827.
- [27] S. Jiang, R. Wang, M. Pang, H. Wang, S. Zeng, X. Yue, L. Ni, Y. Yu, J. Dai, S. Qiu, Z. Zhang, *Electrochim. Acta* 182 (2015) 406–415.
- [28] Z.-S. Wu, G. Zhou, L.-C. Yin, W. Ren, F. Li, H.-M. Cheng, *Nano Energy* 1 (2012) 107–131.
- [29] X.W. Lou, L.A. Archer, *Adv. Mater.* 20 (2008) 1853–1858.
- [30] M.S.A. Sher Shah, A.R. Park, K. Zhang, J.H. Park, P.J. Yoo, *ACS Appl. Mater. Interfaces* 4 (2012) 3893–3901.
- [31] V. Singh, D. Joung, L. Zhai, S. Das, S.I. Khondaker, S. Seal, *Prog. Mater. Sci.* 56 (2011) 1178–1271.
- [32] H. Huang, J. Fang, Y. Xia, X. Tao, Y. Gan, J. Du, W. Zhu, W. Zhang, *J. Mater. Chem. A* 1 (2013) 2495.
- [33] J. Xu, R.D. Deshpande, J. Pan, Y.-T. Cheng, V.S. Battaglia, *J. Electrochem. Soc.* 162 (2015) A2026–A2035.
- [34] Y.-k. Zhou, L. Cao, F.-b. Zhang, B.-l. He, H.-l. Li, *J. Electrochem. Soc.* 150 (2003) A1246.
- [35] Y. Cai, H.-E. Wang, S.-Z. Huang, M.F. Yuen, H.-H. Cai, C. Wang, Y. Yu, Y. Li, W.-J. Zhang, B.-L. Su, *Electrochim. Acta* 210 (2016) 206–214.
- [36] M. Wagemaker, A.P.M. Kentgens, F.M. Mulder, *Nature* 418 (2002) 397–399.
- [37] P. Lian, X. Zhu, S. Liang, Z. Li, W. Yang, H. Wang, *Electrochim. Acta* 55 (2010) 3909–3914.
- [38] W. Zhuang, L. Lu, W. Li, R. An, X. Feng, X. Wu, Y. Zhu, X. Lu, *Chin. J. Chem. Eng.* 23 (2015) 583–589.
- [39] W. Ahn, H.S. Song, S.-H. Park, K.-B. Kim, K.-H. Shin, S.N. Lim, S.-H. Yeon, *Electrochim. Acta* 132 (2014) 172–179.
- [40] A. Li, H. Song, X. Chen, J. Zhou, Z. Ma, *ACS Appl. Mater. Interfaces* 7 (2015) 22372–22379.